

## An Incremental Remapping Transport Scheme on a Spherical Geodesic Grid

WILLIAM H. LIPSCOMB

*Group T-3, Los Alamos National Laboratory, Los Alamos, New Mexico*

TODD D. RINGLER

*Department of Atmospheric Science, Colorado State University, Fort Collins, Colorado*

(Manuscript received 17 August 2004, in final form 9 February 2005)

### ABSTRACT

Weather and climate models contain equations for transporting conserved quantities such as the mass of air, water, ice, and associated tracers. Ideally, the numerical schemes used to solve these equations should be conservative, spatially accurate, and monotonicity-preserving. One such scheme is incremental remapping, previously developed for transport on quadrilateral grids. Here the incremental remapping scheme is reformulated for a spherical geodesic grid whose cells are hexagons and pentagons. The scheme is tested in a shallow-water model with both uniform and varying velocity fields. Solutions for standard shallow-water test cases 1, 2, and 5 are obtained with a centered scheme, a flux-corrected transport (FCT) scheme, and the remapping scheme. The three schemes are about equally accurate for transport of the height field. For tracer transport, remapping is far superior to the centered scheme, which produces large overshoots, and is generally smoother and more accurate than FCT. Remapping has a high startup cost associated with geometry calculations but is nearly twice as fast as FCT for each added tracer. As a result, remapping is cheaper than FCT for transport of more than about seven tracers.

### 1. Introduction

Weather and climate models contain many transport equations of the form

$$\frac{\partial \rho}{\partial t} + \nabla \cdot (\rho \mathbf{u}) = 0, \quad (1)$$

where  $\mathbf{u}$  is the velocity field in two or three dimensions, and  $\rho$  is the density of a fluid such as air or water. Associated with (1) are equations for the transport of passive tracers:

$$\frac{\partial}{\partial t} (\rho T) + \nabla \cdot (\rho T \mathbf{u}) = 0, \quad (2)$$

where  $T$  is the tracer concentration per unit mass. Equations (1) and (2) imply that  $T$  is unchanged along fluid trajectories:

$$\frac{dT}{dt} = \frac{\partial T}{\partial t} + \mathbf{u} \cdot \nabla T = 0, \quad (3)$$

where  $dT/dt$  is the material or Lagrangian derivative.

Transport equations of the form (1) and (2) are solved repeatedly in atmosphere, ocean, and sea ice models. Ocean and atmosphere flows are characterized by a high Reynolds number—that is, a large ratio of advective to frictional terms in the equations of motion. A momentum equation is solved for  $\mathbf{u}$ , and then (1) is solved for the fluid density or layer thickness to find the new mass distribution. Simultaneously, equations of the form (2) are solved to obtain the new distribution of tracers such as temperature, salinity, and chemical species concentrations. Sea ice flows have a low Reynolds number, and sea ice is often modeled as a viscous-plastic material (e.g., Hunke and Dukowicz 1997). The sea ice momentum equation differs from the momentum equations in ocean and atmosphere models, but sea ice transport equations have the same form. Given the velocity field, (1) is solved to find the new concentration of ice area (the sea ice analog of fluid density), and (2) gives the new values of tracers such as ice and snow thickness.

---

*Corresponding author address:* Dr. William H. Lipscomb, Group T-3, MS B216, Los Alamos National Laboratory, Los Alamos, NM 87545.  
E-mail: Lipscomb@lanl.gov

Many numerical methods have been developed for solving transport equations (e.g., LeVeque 1992). Ideally, a numerical method should preserve the properties of the continuous equations it seeks to approximate. One important property is conservation. Equations (1) and (2) are equivalent to the conservation equations

$$\frac{d}{dt} \left( \int_{V_L} \rho dV \right) = 0, \quad (4)$$

$$\frac{d}{dt} \left( \int_{V_L} \rho T dV \right) = 0, \quad (5)$$

where  $dV$  is a volume element, and the integral is taken over a Lagrangian volume  $V_L$  whose bounding surface moves with the local fluid velocity. Numerical transport schemes often are written in terms of fluxes across grid cell faces so that conservation is satisfied automatically. Another important property is monotonicity—the avoidance of unphysical overshoots and undershoots. It is desirable to preserve the monotonicity of tracers as well as density; schemes that preserve tracer monotonicity are said to be compatible (Schär and Smolarkiewicz 1996). Other desirable properties include stability, accuracy, and efficiency. Accuracy of at least second order in space is often needed, since first-order-accurate schemes are very diffusive. If the Courant–Friedrichs–Lewy (CFL) number [defined as  $\max(|\mathbf{u}\Delta t/\Delta x|)$ ] is close to 1, the method should also be at least second-order accurate in time. Computational efficiency is an issue for complex schemes, especially if many tracers are present. It is difficult to design schemes that are simultaneously accurate, monotonicity-preserving, and efficient.

Two simple, inexpensive, conservative schemes are the first-order upwind, or donor cell, scheme and the second-order centered scheme. The donor cell scheme, which approximates the transported field at each cell edge using the upwind value, preserves monotonicity but is highly diffusive. In centered schemes the field is estimated at each edge by averaging the values from the cell centers nearest the edge. Centered differencing conserves variance but violates monotonicity, producing ripples and negative values near steep gradients. More complicated schemes have been developed to provide accuracy without spurious overshoots. One such scheme, flux-corrected transport (FCT; Zalesak 1979), blends the desired properties of low-order and higher-order schemes. The flux across each edge has two components: a low-order flux that preserves monotonicity and a higher-order antidiffusive flux that corrects the truncation error associated with the low-order flux. The two fluxes are weighted such that as much of

the antidiffusive flux is applied as possible without violating monotonicity.

Another method that combines the best properties of low-order and higher-order schemes is incremental remapping, developed by Dukowicz and Baumgardner (2000, henceforth DB) for 2D transport. In this scheme, fluid velocities are projected backward from cell corners to define departure regions. Fields at time level  $n$  are reconstructed over the grid, integrated over the departure regions, and remapped onto the grid at time level  $n + 1$ . Each field is reconstructed with second-order spatial accuracy, except where limited to preserve monotonicity. One advantage of remapping is that it preserves tracer monotonicity without extra work. Also, remapping can efficiently transport large numbers of tracers, since much of the work is geometric and need not be repeated for each field. Lipscomb and Hunke (2004, henceforth LH) showed that incremental remapping is a robust, efficient, accurate scheme for horizontal transport in sea ice models with multiple thickness categories. Remapping is conceptually similar to the cell-integrated semi-Lagrangian (CISL) schemes developed by Machenhauer and colleagues (e.g., Nair and Machenhauer 2002; Nair et al. 2003). In both methods, scalars are integrated over departure regions defined by backward trajectories from cell corners. In CISL schemes, however, the integral is taken over the entire departure cell; in the DB scheme, scalars are integrated only over the part of the cell that is transported across a cell edge.

In most geophysical models the equations of motion are solved for quadrilateral grid cells. The grid lines either follow lines of constant latitude and longitude or are stretched to avoid polar singularities (Smith et al. 1995). Several researchers, however, have built geophysical models on spherical geodesic grids (e.g., Sourdoury et al. 1968; Williamson 1968; Masuda and Ohnishi 1986; Thuburn 1997; Ringler et al. 2000). These grids typically are constructed by dividing the sphere into 12 pentagons and a larger number of hexagons, starting from the icosahedron (Heikes and Randall 1995). Geodesic grids are in some ways better suited for GCMs than are conventional quadrilateral grids. Geodesic grids are highly isotropic: each grid cell is surrounded by five or six nearly equidistant neighbors lying across cell edges, instead of by a mix of edge and corner neighbors. Each geodesic grid cell has nearly the same size and shape, unlike a latitude–longitude grid where cell areas decrease and aspect ratios increase toward the poles. Since geodesic grids have no polar singularities, finite-difference methods can be applied everywhere on the sphere.

Randall et al. (2002) are developing a global climate

model in which each model component—atmosphere, ocean, land, and sea ice—lies on a spherical geodesic grid. The ocean, land, and sea ice models share a surface grid. The atmospheric grid has the same shape as the surface grid but typically a coarser resolution. The atmosphere and ocean components have quasi-Lagrangian vertical coordinates so that vertical advection is minimized and fluid motions are nearly two-dimensional. Layer thicknesses evolve in time and are periodically remapped onto a target vertical grid. Because the layer thickness can have large horizontal gradients, care must be taken during horizontal transport to ensure that mass remains positive.

Incremental remapping appears well suited for horizontal transport in such a climate model. For quasi-horizontal fluid motions a 3D transport scheme is not needed, and a 2D scheme will suffice. Upwind transport is too diffusive, and centered differencing is highly oscillatory. FCT is accurate and monotonicity-preserving, but is relatively expensive in models with many tracers. Historically, climate models have carried only a few prognostic tracers: temperature and salinity in the ocean, one or more phases of water in the atmosphere, and thickness and temperature in one or two sea ice thickness categories. This is no longer the case. Atmospheric chemistry models, ocean biogeochemistry models, and multicategory sea ice models typically carry 10 to 100 tracers. Remapping could efficiently solve the problem of transporting many tracers accurately.

Incremental remapping has not previously been applied on a geodesic grid. In this paper we describe a remapping scheme for spherical geodesic grids and use it to compute fluid transport in a shallow-water model. Since the shallow-water equations are similar to the equations for horizontal flow in a 3D model, this application is a first step toward using incremental remapping in isentropic ocean and atmosphere models. Section 2 describes the spherical geodesic grid, and section 3 explains how incremental remapping is done on this grid. Section 4 sets forth the shallow-water equations and describes the solution method. Section 5 presents results from three standard shallow-water test cases and compares remapping to centered and FCT schemes. Conclusions are given in section 6.

## 2. The spherical geodesic grid

A spherical geodesic grid can be generated by repeated subdivision of the 20 triangular faces of an icosahedron (Heikes and Randall 1995). Figure 1 shows how the grid is formed by recursive bisection and projection. First, each edge is bisected to form four smaller triangles on each face; then the triangle vertices are pro-

jected to the surface of the sphere. This process is repeated to yield progressively finer grids. A Voronoi tessellation is then defined as the set of points closer to a particular vertex than to any other vertex. After the spherical Voronoi tessellation is obtained at the target resolution, the tessellation is modified slightly such that the center of each face coincides with the centroid of that grid cell. Du et al. (1999) have shown that in many cases centroidal Voronoi tessellations are optimal tessellations.

The grid cells are hexagons, except for 12 pentagons lying at the 12 vertices of the original icosahedron. The grid is oriented with 2 pentagons at the poles and the other 10 pentagons in midlatitudes. The number of grid cells for a given recursion level  $R$  is given by

$$N = 5 \cdot 2^{2R+3} + 2, \quad (6)$$

where  $R = -1$  corresponds to the original icosahedron. The grids used in this paper correspond to  $R = 3, 4, 5,$  and  $6$ , with  $N = 2562, 10242, 40\,962,$  and  $163\,842$ , respectively. With  $N = 2562$  the average distance between cell centers is 481.6 km, giving a resolution of about  $4.5^\circ$  at the equator. This distance is halved with each increase in resolution.

It is convenient to store grid cell data in logically rectangular 2D arrays in which the closest neighbors on the grid are also neighbors in computer memory. This is done by dividing the grid into five equally shaped panels (Fig. 2). Each panel consists of four adjacent spherical triangles corresponding to four faces of the initial icosahedron. On each panel the arrangement of grid cells is logically rectangular. The panel dimensions are extended by one cell in each direction to include ghost cells (i.e., neighboring cells belonging to other panels) and the two poles. Each panel can be further divided and the subblocks distributed over many processors in order to exploit parallel computer architectures.

The number of vertices  $V$  and edges  $E$  is related to the number of faces  $F$  by Euler's formula:

$$F + V - E = 2. \quad (7)$$

At the  $R = 3$  recursion level, for example, the grid has 2562 faces, 5120 vertices, and 7680 edges. If the faces corresponding to the two poles are excluded, then two vertices and three edges can be associated uniquely with each face. Consider the central hexagon in Fig. 3. By convention, this hexagon owns the west, southwest, and southeast edges, along with the two vertices that bound the southwest edge. The neighboring grid cells are indexed as shown in the figure. The indexing is similar to that on a rectangular grid, except that the cell has six neighbors instead of eight, and the  $(i - 1, j + 1)$  and  $(i + 1, j - 1)$  grid cells do not border cell

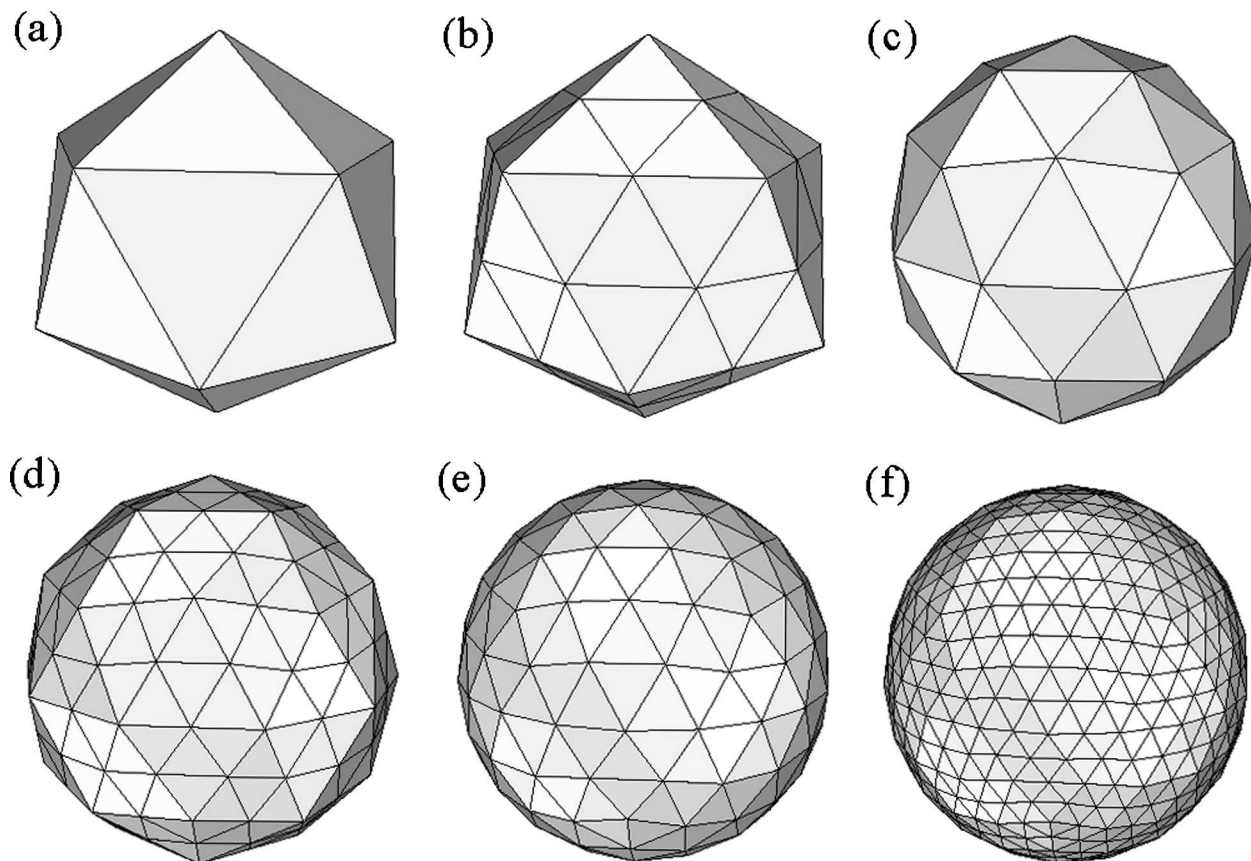


FIG. 1. Generating geodesic grids by recursive bisection and projection.

$(i, j)$ . The indexing is modified slightly for neighbors of pentagons. More details can be found online at <http://kiwi.atmos.colostate.edu/BUGS/geodesic>.

It is convenient to define several coordinate systems, denoted by  $X1$ ,  $X2$ ,  $X3$ , and  $X4$ . System  $X1$  is a global 3D Cartesian coordinate system whose origin lies at the center of the earth, with the  $x$  and  $y$  axes passing through the equator and the positive  $z$  axis intersecting the North Pole. Systems  $X2$ ,  $X3$ , and  $X4$  are local 2D coordinate systems defined at each vertex, cell center, and edge midpoint, respectively. System  $X2$ , which is defined at each vertex, lies in the plane formed by joining the centers of the three faces surrounding the vertex. Its  $x$  and  $y$  axes point in the local east and north directions. System  $X3$  is defined at each cell center and lies in a plane that passes as close as possible to the five or six cell corners, with its  $x$  and  $y$  axes pointing eastward and northward as in  $X2$ . Finally,  $X4$  is defined for each edge, with its origin at the midpoint of the edge, the  $x$  axis lying along the edge, and the  $y$  axis perpendicular to the edge. Vectors are transformed among these four coordinate systems by matrix multiplication. Transformations between  $X1$  and the 2D coordi-

nate systems are done directly, whereas transformations between two 2D systems are carried out via an intermediate transformation to  $X1$ . Since neighboring 2D coordinate systems are not quite coplanar, a vector in one system has a small component perpendicular to the plane of the neighboring system. In the vector transformations described below, this perpendicular component is discarded, resulting in a small spatial discretization error.

The equations of motion are discretized on the Z/ZM grid (Ringer and Randall 2002a,b), in which scalars are located at cell centers and vectors at cell corners. Ringer and Randall (2002a, henceforth RR) defined discrete divergence, gradient, curl, and Laplacian operators that retain important properties of their continuous counterparts. Equations (1) and (2) contain the scalar divergence operator, which is discretized by RR as

$$(\nabla \cdot \mathbf{u})_i = \frac{1}{A_i} \sum_{c=1}^{nc} (F_{c^+} + F_{c^-}), \quad (8)$$

where

$$F_{c^+} \equiv \mathbf{u}_c \cdot \mathbf{n}_c + d_{c^+} \quad \text{and} \quad F_{c^-} \equiv \mathbf{u}_c \cdot \mathbf{n}_c - d_{c^-}. \quad (9)$$

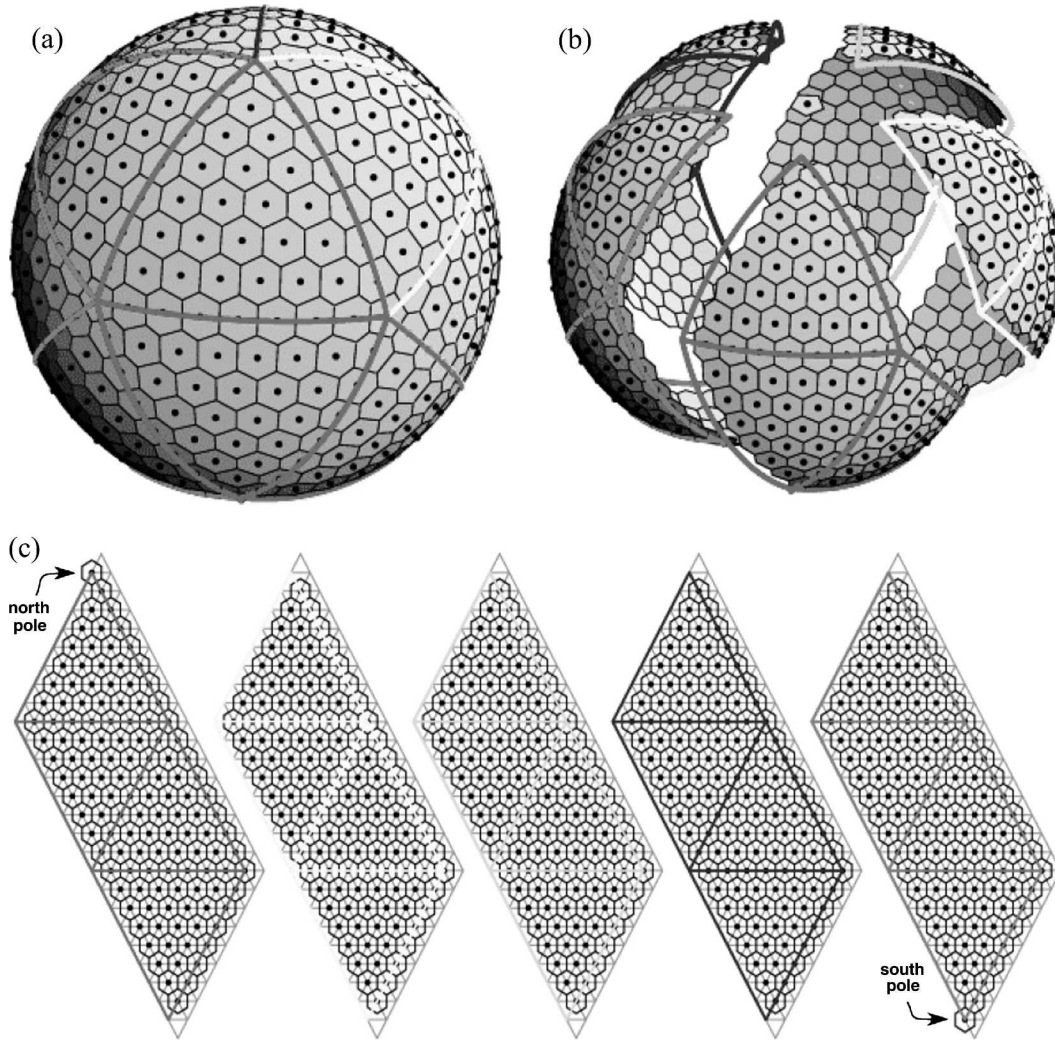


FIG. 2. The geodesic grid consists of 20 spherical triangles corresponding to the 20 faces of the original icosahedron. (a) Spherical triangles overlying a low-resolution grid. (b) The grid is separated into five panels of four triangles each. (c) The panels are stretched to show that each panel is logically rectangular.

Here,  $A_i$  is the grid cell area,  $\mathbf{u}_c$  is the velocity in  $X2$  coordinates at corner  $c$ ,  $nc$  is the total number of corners (5 or 6),  $\mathbf{n}_{c^+}$  and  $\mathbf{n}_{c^-}$  are unit vectors normal to the cell edges, and  $d_{c^+}$  and  $d_{c^-}$  are lengths of half-edges, as shown in Fig. 4. The  $c^+$  direction is counterclockwise from corner  $c$ , and  $c^-$  is clockwise. To find the divergence of a product of a scalar and a vector, such as  $\rho \mathbf{u}$  in (2),  $\rho$  must be averaged to the cell corners. The reader may refer to RR for definitions of the gradient, curl, Laplacian, and averaging operators.

### 3. Incremental remapping on a geodesic grid

We now describe the incremental remapping algorithm, emphasizing features specific to geodesic grids. More details can be found in DB and LH.

Given a 2D velocity field  $\mathbf{u}$ , we wish to update the density field  $\rho$  and associated tracer concentration fields  $T$  that evolve according to (1) and (2). Scalars are located at cell centers and velocity vectors at cell corners. Incremental remapping proceeds in four stages:

- 1) Given the mean value of the density and tracer in each cell at time level  $n$ , approximate the density and tracer fields as linear functions of  $x$  and  $y$ . Limit the field gradients as needed to preserve monotonicity.
- 2) Given the velocity at cell corners, locate the departure regions from which material is transported across the edges of each grid cell. Divide these regions into triangles and find the vertices of each triangle.

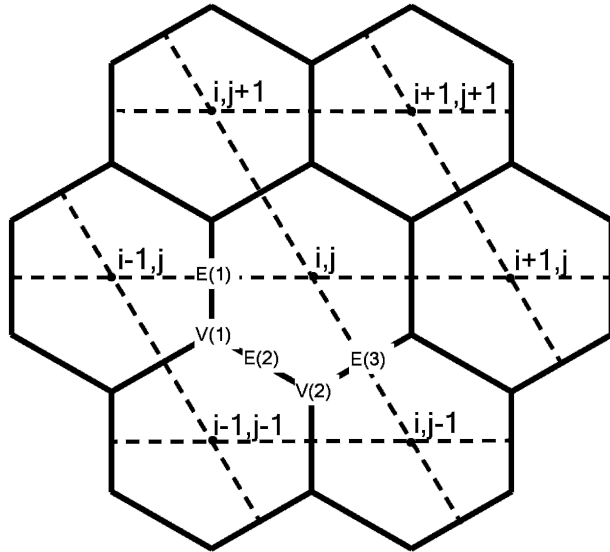


FIG. 3. Indexing of grid cells on the geodesic grid. The oblique dashed lines pass through values of constant  $i$ , and the horizontal dashed lines through values of constant  $j$ . Cell  $(i, j)$  owns the edges to the west [E(1)], southwest [E(2)], and southeast [E(3)]. Cell  $(i, j)$  also owns the vertices bounding the southwest edge [V(1) and V(2)].

- 3) Integrate over the departure triangles to determine the mass transported across each cell edge.
- 4) Compute the mass entering and leaving each grid cell, and update the mean density and tracer values to time level  $n + 1$ .

Since the velocity is the same for each transported field, the departure triangles in step (2) are computed just once per time step. The other three steps are repeated for each field.

This process is illustrated in Fig. 5. The target grid consists of regular hexagons, and the irregular shaded hexagon is the departure region associated with the central target hexagon. The arrows lie along the local velocity field and must not extend beyond the nearest neighbors of the target hexagon; this is what is meant by incremental as opposed to general remapping. For stability, the arrows must not cross one another. The material contained in the shaded hexagon at time level  $n$  is assumed to arrive in the target hexagon at time level  $n + 1$ . The density and tracer fields in the target hexagon are updated by computing the mass transported across each edge. The algorithm is described in detail below.

*a. Reconstructing density and tracer fields*

First, the density field  $\rho$  and tracer fields  $T$  at time level  $n$  are reconstructed in each grid cell as functions of  $\mathbf{r} = (x, y)$  in coordinate system  $X3$ , whose origin lies at the cell center. The mean density and tracer are  $\bar{\rho}$  and

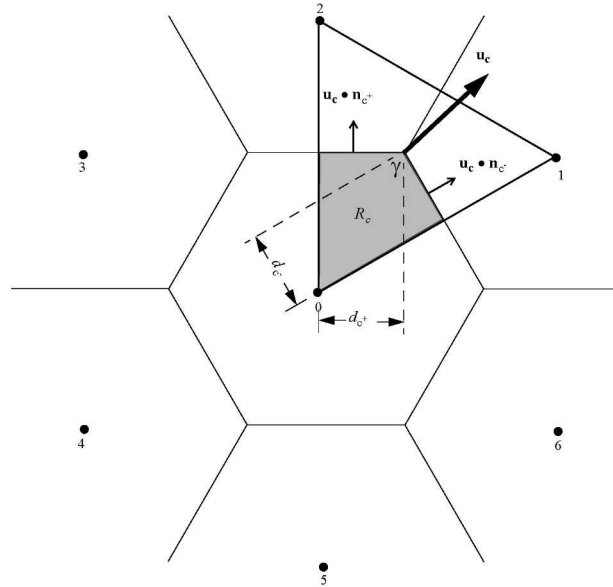


FIG. 4. Quantities associated with the discrete divergence operator. Vectors are defined at cell corners and scalars at cell centers. The velocity at the corner is  $\mathbf{u}_c$ ;  $d_{c^+}$  and  $d_{c^-}$  are lengths of half-edges; and  $\mathbf{n}_{c^+}$  and  $\mathbf{n}_{c^-}$  are unit vectors normal to cell edges, where  $c^+$  denotes the counterclockwise direction from the cell corner and  $c^-$  the clockwise direction. The cell area  $A_i$  is defined by the perimeter of the hexagon.

$\bar{T}$ , respectively; these are the prognostic variables stored in computer memory. The reconstructed density and tracer fields, when integrated over the grid cell, must have means  $\bar{\rho}$  and  $\bar{T}$ :

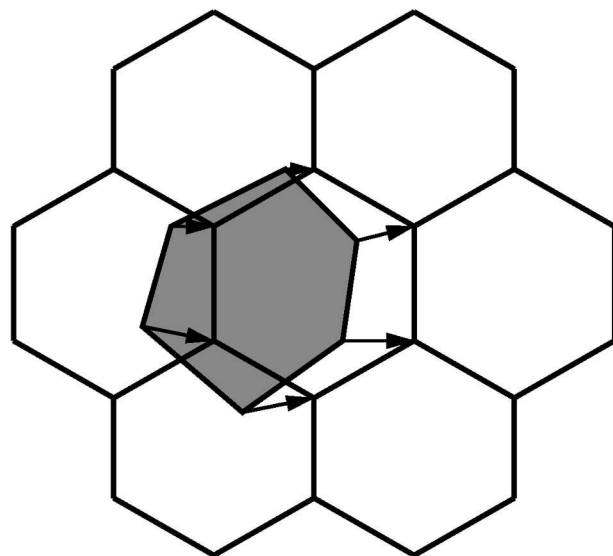


FIG. 5. Incremental remapping on the geodesic grid. Conserved quantities contained in the shaded hexagon at time level  $n$  arrive in the central target hexagon at time level  $n + 1$ . The arrows denote backward trajectories computed from the cell corner velocities.

$$\int_A \rho(\mathbf{r}) dA = \bar{\rho}A, \quad (10)$$

$$\int_A \rho(\mathbf{r})T(\mathbf{r}) dA = \bar{\rho}\bar{T}A, \quad (11)$$

where  $A$  is the grid cell area. Equation (10) is satisfied if  $\rho(\mathbf{r})$  has the form

$$\rho(\mathbf{r}) = \bar{\rho} + \alpha_p \langle \nabla \rho \rangle \cdot (\mathbf{r} - \bar{\mathbf{r}}), \quad (12)$$

where  $\langle \nabla \rho \rangle$  is the cell-centered density gradient,  $\alpha_p$  is a coefficient between 0 and 1 that preserves monotonicity, and  $\bar{\mathbf{r}}$  is the cell centroid. Similarly, (11) is satisfied if  $T(\mathbf{r})$  is given by

$$T(\mathbf{r}) = \bar{T} + \alpha_T \langle \nabla T \rangle \cdot (\mathbf{r} - \bar{\mathbf{r}}), \quad (13)$$

where  $\bar{\mathbf{r}}$  is the center of mass. The centroids are pre-computed and stored, and the centers of mass are evaluated at each time step. For the centroidal Voronoi tessellations used in this paper,  $\bar{\mathbf{r}} = 0$  in each grid cell. The gradients  $\nabla \rho$  and  $\nabla T$  are computed at cell corners as in RR, and then averaged to cell centers. These gradients are limited, if necessary, so that the maximum and minimum values of  $\rho(\mathbf{r})$  and  $T(\mathbf{r})$  in each cell are in the range of the mean values in the cell and its nearest neighbors. This procedure, based on van Leer (1979), is sufficient to preserve monotonicity. A linear reconstruction of scalar fields gives a numerical scheme that is second-order accurate in space. With van Leer limiting, the accuracy is formally reduced to first order, but if the limiting is confined to a small fraction of grid cells at any given time, the scheme may converge in practice with close to second-order accuracy.

### b. Locating departure triangles

The next step is to locate the vertices of the departure regions associated with each cell edge. The departure regions are quadrilaterals whose four vertices are the two cell corners bounding the cell edge, along with the endpoints of the backward trajectories associated with these corners. Each departure quadrilateral is partitioned into two or more triangles, with the rule that each triangle must lie entirely within a single grid cell. We first describe the procedure for finding departure points, then show how to find the vertices of the departure triangles.

The velocity at each grid cell corner is known in  $X2$  coordinates. The simplest way to find departure points  $\mathbf{x}_d$  is to project the velocity directly backward in time from the cell corner:

$$\mathbf{x}_d = \mathbf{x}_0 - \mathbf{u}_0 \Delta t, \quad (14)$$

where  $\mathbf{x}_0$  is the corner location and  $\mathbf{u}_0$  is the corner velocity. This method is first-order accurate. A second-order-accurate procedure is to estimate the trajectory midpoint,  $\mathbf{x}_m = \mathbf{x}_0 - \mathbf{u}_0 \Delta t/2$ , then approximate the velocity  $\mathbf{u}_m$  at the midpoint and replace  $\mathbf{u}_0$  with  $\mathbf{u}_m$  in (14). Let the three neighboring corners be denoted by  $\mathbf{x}_1$ ,  $\mathbf{x}_2$ , and  $\mathbf{x}_3$ , and suppose  $\mathbf{x}_m$  lies in a triangle whose vertices are  $\mathbf{x}_0$ ,  $\mathbf{x}_1$ , and  $\mathbf{x}_2$ . The midpoint velocity can be interpolated from the vertices using

$$\mathbf{u}_m = \mathbf{u}_0 + \alpha(\mathbf{u}_1 - \mathbf{u}_0) + \beta(\mathbf{u}_2 - \mathbf{u}_0), \quad (15)$$

where  $\alpha$  and  $\beta$  are the solutions of

$$\mathbf{x}_m = \mathbf{x}_0 + \alpha(\mathbf{x}_1 - \mathbf{x}_0) + \beta(\mathbf{x}_2 - \mathbf{x}_0). \quad (16)$$

In (15) and (16), all vectors lie in the  $X2$  coordinate system located at  $\mathbf{x}_0$ . The accuracy of the backward trajectories can be improved by iterating the midpoint method or by using the noniterative scheme of McGregor (1993), as applied on the geodesic grid by Giraldo (1999). For the test problems below, these refinements do not significantly change the results.

Given the departure points, the quadrilateral departure region is divided into one or more triangles, each of which encloses material transported across the edge from a single grid cell (Fig. 6). The departure region lies in up to four grid cells: the two cells ( $T$  and  $B$ ) that border the cell edge, and the two cells ( $L$  and  $R$ ) that contain an endpoint of the edge. This region can contain at most four triangles: one each in cells  $L$  and  $R$ , and two in cells  $T$  and  $B$  combined. The appendix describes in detail the procedure for finding the vertices of departure triangles.

Each grid cell (except the two pole cells) owns three edges; for each edge there are up to four departure triangles, and each triangle has three vertices. Thus the 2D positions of  $3 \times 4 \times 3 = 36$  vertices are stored for each grid cell. These vertices are computed initially in  $X4$  and then transformed to the  $X3$  coordinates of the cell contributing the transport. The area and sign of each departure triangle are also computed. If the vertices are  $\mathbf{x}_i = (x_i, y_i)$ ,  $i \in \{1, 2, 3\}$ , the triangle area  $A_T$  is given by

$$A_T = \frac{1}{2} |(x_2 - x_1)(y_3 - y_1) - (y_2 - y_1)(x_3 - x_1)|. \quad (17)$$

By convention, flows directed out of the cell that owns the edge are positive, and flows into that cell are negative.

### c. Integrating the transport

Next the transported mass is integrated over each departure triangle for each conserved field. Polynomial

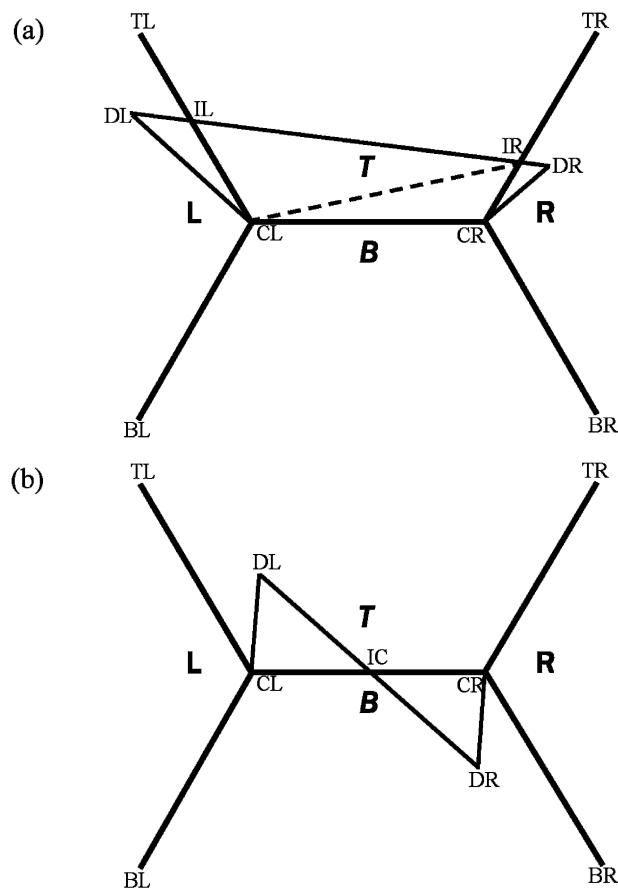


FIG. 6. To compute the transport across the edge joining CL and CR, the departure points DL and DR are connected to each other and to their respective arrival points. The figure shows two of many possible geometric configurations: (a) a triangle in the left cell (L), a triangle in the right cell (R), and a quadrilateral in the top cell (T), and (b) triangles in cell T and in the bottom cell (B). See the appendix for a complete discussion.

functions can be integrated exactly over triangles using simple cubature formulas (Stroud 1971). The integrals of linear, quadratic, and cubic functions  $f(\mathbf{x})$  over a triangle with vertices  $\mathbf{x}_i$  and area  $A_T$  are given, respectively, by

$$I_1 = A_T f(\mathbf{x}_0), \quad (18)$$

$$I_2 = \frac{A_T}{3} \sum_i f(\mathbf{x}_i), \quad (19)$$

$$I_3 = A_T \left[ -\frac{9}{16} f(\mathbf{x}_0) + \frac{25}{48} \sum_i f(\mathbf{x}_i'') \right], \quad (20)$$

where  $\mathbf{x}_0$  is the triangle midpoint,

$$\mathbf{x}_0 = \frac{1}{3} \sum_i \mathbf{x}_i, \quad (21)$$

and the cubature points in (19) and (20) are  $\mathbf{x}_i' \equiv (\mathbf{x}_0 + \mathbf{x}_i)/2$  and  $\mathbf{x}_i'' \equiv (3\mathbf{x}_0 + 2\mathbf{x}_i)/5$ . Suppose the transported fields are  $\rho$  and  $\rho T$  as in (1) and (2). Then  $\rho$ , a linear function of  $x$  and  $y$ , can be integrated exactly using (18), and  $\rho T$ , a quadratic function, using (19). Equation (20) can be used to integrate the product of a density and two tracers: for example, the internal energy of sea ice, which is a product of ice area, thickness, and enthalpy. In practice, it may be possible to integrate quadratic and cubic functions using (18) instead of (19) or (20) with little loss of accuracy.

#### d. Updating mass and tracer fields

Given the mass transports  $m_k$  and mass-weighted tracer transports  $(mT)_k$  across each edge  $k$  of a grid cell with area  $A$ , the values of  $\rho$  and  $T$  at time level  $n+1$  are given by

$$\rho^{n+1} = \rho^n - \frac{1}{A} \sum_k \pm m_k, \quad (22)$$

$$T^{n+1} = \frac{\rho^n T^n - \frac{1}{A} \sum_k \pm (mT)_k}{\rho^{n+1}}. \quad (23)$$

Following the sign convention above, the positive sign is taken for transports across the three edges owned by the cell and the negative sign for the other edges. Dukowicz and Baumgardner (2000) showed that (23) satisfies tracer compatibility, since the new-time tracer is a density-weighted average of old-time values over the departure region.

## 4. The shallow-water equations

We wish to evaluate incremental remapping as a scheme for mass and tracer transport in geophysical models on a spherical geodesic grid. To this end we solve the frictionless shallow-water equations, which describe 2D motion of a single layer of fluid under the influence of gravity and the Coriolis force. Following RR, these equations can be written as

$$\frac{\partial \mathbf{u}}{\partial t} = -\eta \mathbf{k} \times \mathbf{u} - \nabla[K + g(h + h_s)], \quad (24)$$

$$\frac{\partial h}{\partial t} = -\nabla \cdot (h\mathbf{u}), \quad (25)$$

$$\frac{\partial}{\partial t} (hT) = -\nabla \cdot (hT\mathbf{u}), \quad (26)$$

where  $h$  is the fluid depth,  $h_s$  is the surface height,  $g$  is the gravitational constant,  $K = \mathbf{u} \cdot \mathbf{u}/2$  is the kinetic energy,  $\mathbf{k}$  is the vertical unit vector, and  $\eta = f + \mathbf{k} \cdot \nabla$

$\times \mathbf{u}$  is the absolute vorticity (where  $f$  is the Coriolis parameter). Equation (24) is the momentum equation, and (25) and (26) are transport equations analogous to (1) and (2). This form of the shallow-water equations is known as the momentum formulation. Taking the curl and divergence of (24) results in equations for the vorticity and divergence:

$$\frac{\partial \eta}{\partial t} = -\nabla \cdot (\eta \mathbf{u}), \quad (27)$$

$$\frac{\partial \delta}{\partial t} = \mathbf{k} \cdot \nabla \times (\eta \mathbf{u}) - \nabla^2 [K + g(h + h_s)], \quad (28)$$

where  $\delta = \nabla \cdot \mathbf{u}$  is the divergence. The vorticity and divergence are related to the velocity by

$$\eta = \nabla^2 \psi, \quad (29)$$

$$\delta = \nabla^2 \chi, \quad (30)$$

where  $\psi$  is the streamfunction,  $\chi$  is the velocity potential, and

$$\mathbf{u} = \mathbf{k} \times \nabla \psi + \nabla \chi. \quad (31)$$

Equations (25)–(28) are known as the vorticity-divergence form of the shallow-water equations; they are equivalent to the momentum formulation in the continuous limit. In this paper the equations are solved using the vorticity-divergence formulation, which eliminates the computational modes permitted by the momentum formulation.

The shallow-water equations must be discretized on the geodesic grid. The scalar quantities associated with each grid cell  $i$  include the fluid thickness  $h_i$ , surface height  $h_{si}$ , tracer concentration  $T_i$ , absolute vorticity  $\eta_i$ , potential vorticity  $q_i = \eta_i/h_i$ , potential enstrophy  $q_i^2$ , kinetic energy  $K_i$ , and potential energy  $g(h_{si} + h_i/2)$ . Ideally, a discretization should conserve as many as possible of the infinitely many quantities conserved by the continuous equations. Ringler and Randall (2002a) defined discrete operators that guarantee conservation of global mass, mass-weighted tracer, mass-weighted potential vorticity, mass-weighted tracer variance, mass-weighted potential enstrophy, and total (kinetic plus potential) energy. Mass, mass-weighted tracer, and mass-weighted potential vorticity are conserved simply by writing the transport Eqs. (25)–(27) in flux form. [Note that (27) has the same form as (26) when  $hq$  is substituted for  $\eta$ .] Tracer variance, potential enstrophy, and total energy are conserved provided that  $T$ ,  $q$ , and  $h$  are averaged to cell edges and corners as described in RR.

In the RR scheme the shallow-water equations are integrated in time using the third-order Adams–Bash-

forth method (AB3; Durran 1991). The value of a field  $\phi$  at time level  $n + 1$  is given by

$$\phi_{n+1} = \phi_n + \Delta t \left( \frac{23}{12} \phi'_n - \frac{4}{3} \phi'_{n-1} + \frac{5}{12} \phi'_{n-2} \right), \quad (32)$$

where the  $\phi'$  are tendencies at three successive time levels. Assuming that the tendencies at time levels  $n - 1$  and  $n - 2$  have already been computed and stored, the algorithm proceeds as follows. First, the thickness field is advanced using (25) and (32); the discrete divergence of  $h\mathbf{u}$  in (25) is computed using (8) and (9). Tracers are integrated analogously. Next,  $K$  is obtained from the velocity; the various discrete operators are used to evaluate the tendency terms in (27) and (28); and  $\eta$  and  $\delta$  are stepped forward using (32). Then (29) and (30) are inverted to find the streamfunction  $\psi$  and velocity potential  $\chi$  using an elliptic solver (Heikes and Randall 1995). The new velocity is obtained by differentiating  $\psi$  and  $\chi$ .

This solution scheme is second-order accurate in space and has excellent conservation properties. As RR showed, it is well suited for computing the shallow-water thickness field, which is smooth everywhere, never approaches zero, and is controlled by the dynamics. However, centered transport is unsuitable for fields with sharp gradients, especially tracer fields that are not restored dynamically.

For the standard divergence operator used in (25) and (26), the transport across each edge is computed using the centered average thickness and tracers. By replacing these centered averages with the values in the grid cell upwind of each edge, one obtains an upwind divergence operator. The resulting transport scheme is monotone but is too diffusive for most applications. A more accurate scheme is obtained if the first-order upwind and second-order centered fluxes are combined in an FCT scheme, following Smolarkiewicz (1991). The resulting scheme limits the higher-order fluxes so that monotonicity is preserved, provided the transport equations are integrated forward in time. With AB3 time differencing, monotonicity is no longer guaranteed, but the solutions are much smoother than those given by the centered scheme.

Incremental remapping can also be used to solve the transport equations in the shallow-water model. Remapping was applied by DB and LH as a two-time-level scheme, with density and tracer fields advanced from level  $n$  to  $n + 1$  as described in section 3. However, remapping is easily incorporated in a multilevel AB3 scheme. The new thickness and tracer fields given by remapping,  $\tilde{h}_{n+1}$  and  $\tilde{T}_{n+1}$ , are used to evaluate the right-hand sides of (25) and (26):

$$\frac{\partial h}{\partial t} = \frac{\tilde{h}_{n+1} - h_n}{\Delta t}, \quad (33)$$

$$\frac{\partial}{\partial t}(hT) = \frac{\tilde{h}_{n+1}\tilde{T}_{n+1} - h_n T_n}{\Delta t}, \quad (34)$$

where a tilde denotes a temporary value. These tendencies are stored at three time levels and are used in (32) to find  $h_{n+1}$  and  $T_{n+1}$ , the actual values at the new time level. With AB3 time stepping, this scheme is not formally monotone but is very nearly so in practice. When run as a two-time-level scheme, remapping is unstable in combination with the AB3 momentum solver.

## 5. Shallow-water test cases

We now apply these three solution schemes—the RR scheme with centered differencing, the FCT scheme, and incremental remapping—to standard test problems. We consider three of the seven test cases proposed by Williamson et al. (1992) for evaluating numerical solutions of the shallow-water equations on a sphere. The first problem, known as shallow-water test case 1 (SWTC1), tests pure advection by an unchanging, nondivergent velocity field. The second problem, shallow-water test case 2 (SWTC2), consists of steady-state zonal flow. Finally, shallow-water test case 5 (SWTC5) consists of initially zonal flow impinging on a midlatitude mountain. Each scheme was run at four resolutions ( $N = 2562, 10\,242, 40\,962,$  and  $163\,842$ ) with a time step  $\Delta t = 50$  s, close to the maximum stable step for the finest resolution.

When the thickness is controlled dynamically, we would expect the centered scheme to give an accurate thickness field but oscillatory tracer fields. The FCT scheme should generate a thickness field similar to that given by the centered scheme, along with nearly monotone tracer fields. If the incremental remapping scheme is to prove useful, it should produce thickness and tracer fields at least as accurate as those given by FCT, but more efficiently than FCT when many tracers are present. As shown below, remapping satisfies these requirements.

### a. Shallow-water test case 1

SWTC1 tests the advective component of the shallow-water model in isolation. The steady, nondivergent wind field is given by

$$u = u_0(\cos\theta \cos\alpha + \sin\theta \cos\lambda \sin\alpha), \quad (35)$$

$$v = -u_0 \sin\lambda \sin\alpha, \quad (36)$$

where  $\theta$  is latitude,  $\lambda$  is longitude, and  $\alpha$  is the angle between the axis of solid-body rotation and the earth's rotation axis. The maximum speed  $u_0 = 2\pi a/(12 \text{ days})$ , where  $a$  is the earth's radius. On a geodesic grid the results are insensitive to the value of  $\alpha$ ; we set  $\alpha = 0$  in the tests described below. Two shapes are advected. First, following Williamson et al. (1992), we advect a cosine bell whose initial height is

$$h = \left(\frac{h_0}{2}\right) \left[1 + \cos\left(\frac{\pi r}{R}\right)\right] \quad (37)$$

for all points within a distance  $r < R$  of the bell's center on the equator, and  $h = 0$  elsewhere. We set  $h_0 = 1000$  m and  $R = a/3$ . Next, following Zalesak (1979), we advect a slotted cylinder of initial height  $h_0 = 1000$  m and radius  $R = a/2$ , also centered on the equator. We set  $h = 0$  for  $r > R$  and also in a slot of width  $a/6$  and length  $5a/6$ , with the long axis perpendicular to the equator. Because of the sharp discontinuities at the perimeter, the slotted cylinder is a harder test for advection schemes than the cosine bell. The model was run using each scheme at each resolution for 12 days, at the end of which a perfect scheme would give a solution exactly equal to the initial condition.

Solutions can be compared quantitatively by computing the  $L_2$  and  $L_\infty$  error norms. The  $L_2$  norm is the area-weighted rms thickness error, normalized by the area-weighted rms thickness:

$$L_2 = \frac{\sqrt{\sum A_i (h_i - \hat{h}_i)^2}}{\sqrt{\sum A_i \hat{h}_i^2}}, \quad (38)$$

where  $\hat{h}_i$  is the exact thickness in grid cell  $i$  and the summation is over all grid cells. The  $L_\infty$  norm is the maximum thickness error, normalized by the maximum thickness:

$$L_\infty = \frac{\max|h_i - \hat{h}_i|}{\max|\hat{h}_i|}. \quad (39)$$

In theory, each doubling of resolution should reduce the norms by a factor of 2 for first-order-accurate schemes and by a factor of 4 for second-order-accurate schemes. Both norms increase smoothly during the 12-day run. Figure 7 shows how the  $L_2$  norm at the end of 12 days varies with grid resolution for each scheme. At the three lower resolutions, remapping is the most accurate scheme for both the cosine bell and the slotted cylinder, followed by FCT; the centered scheme is least accurate. At the highest resolution, remapping and FCT are about equally accurate. The convergence rates for the cosine bell generally lie between first-order and second-order. For the slotted cylinder the convergence

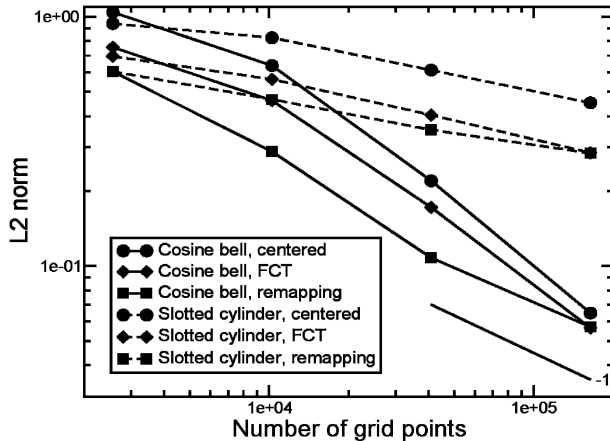


FIG. 7. SWTC1  $L_2$  error norms for advection of a cosine bell (solid lines) and slotted cylinder (dashed lines), as given by the centered, FCT, and remapping schemes. A line of slope  $-1$ , corresponding to first-order accuracy, is shown for reference.

rates are slower than first-order. This slow convergence results from the height discontinuity, which becomes sharper as the distance between neighboring grid cells decreases. The  $L_\infty$  norms (not shown) are similar; remapping is the most accurate scheme for both shapes and at all resolutions.

Figure 8 shows equatorial cross sections of the 12-day solutions with  $N = 40\,962$  for both shapes and each scheme, along with the exact solutions. All three schemes are reasonably good at preserving the shape of the cosine bell, although the centered scheme is non-monotone at the trailing edge. Remapping allows more peak clipping than the other schemes, but also has the smallest phase error. For the slotted cylinder the oscillations given by the centered scheme are more pronounced, with a maximum thickness of 1778 and a minimum of  $-433$ . The remapping and FCT solutions are both of good quality and very nearly monotone, but remapping does better at keeping the slot centered. Figure 9 shows the slotted cylinder solutions in color, again with  $N = 40\,962$ . Remapping (Fig. 9d) does the best job of preserving the initial shape. The FCT solution (Fig. 9c) is smooth and monotone, but with distortions along the trailing edge. Figure 9b vividly illustrates the oscillations in the centered solution. The results at other resolutions are qualitatively similar.

If either the bell or the cylinder were a positive-definite geophysical field, frequent ad hoc corrections would be needed to remove the negative values in the centered solution. These corrections would reduce the formal accuracy of the centered scheme. For the FCT and remapping schemes, negative values arise occasionally because of the AB3 time stepping, but are so small

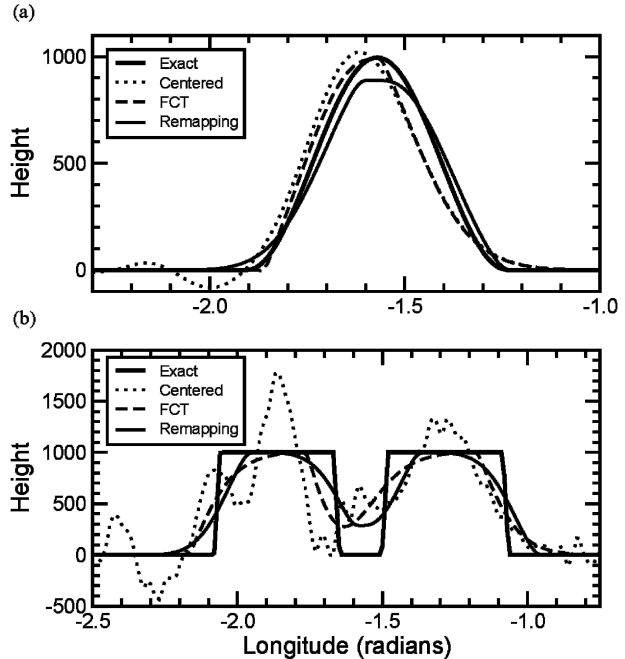


FIG. 8. Equatorial cross sections of the SWTC1 thickness field with  $N = 40\,962$  after one revolution, as given by the centered scheme (dotted lines), FCT (dashed lines), and remapping (thin solid lines). The exact solutions (thick solid lines) are shown for reference. (a) Cosine bell. (b) Slotted cylinder.

that corrections, if needed, would have little effect on the solutions.

#### b. Shallow-water test case 2

In SWTC2 the flow is zonal and in geostrophic balance with the thickness field. The initial velocity field is given by (35) and (36) with  $\alpha = 0$ . The initial thickness field is

$$h = h_0 - \frac{1}{g} \left( a\Omega u_0 + \frac{u_0^2}{2} \right) \sin^2 \theta, \quad (40)$$

where  $\Omega$  is the earth's angular velocity,  $u_0 = 2\pi a/(12 \text{ days})$ , and  $h_0 = 5960 \text{ m}$ . With a perfect numerical scheme,  $\mathbf{u}$  and  $h$  would not change in time.

The resulting thickness errors, as measured by the departure from (40), are very small. Figure 10 shows how the  $L_2$  and  $L_\infty$  norms vary with grid resolution for each scheme. These error norms are computed once per day and averaged over 12 days. (For this test case the norms do not increase smoothly after the first day but fluctuate randomly.) For all three schemes the plotted slope is close to  $-2$ , the expected value for second-order schemes on a log-log scale. The three schemes have nearly the same errors, except that remapping is

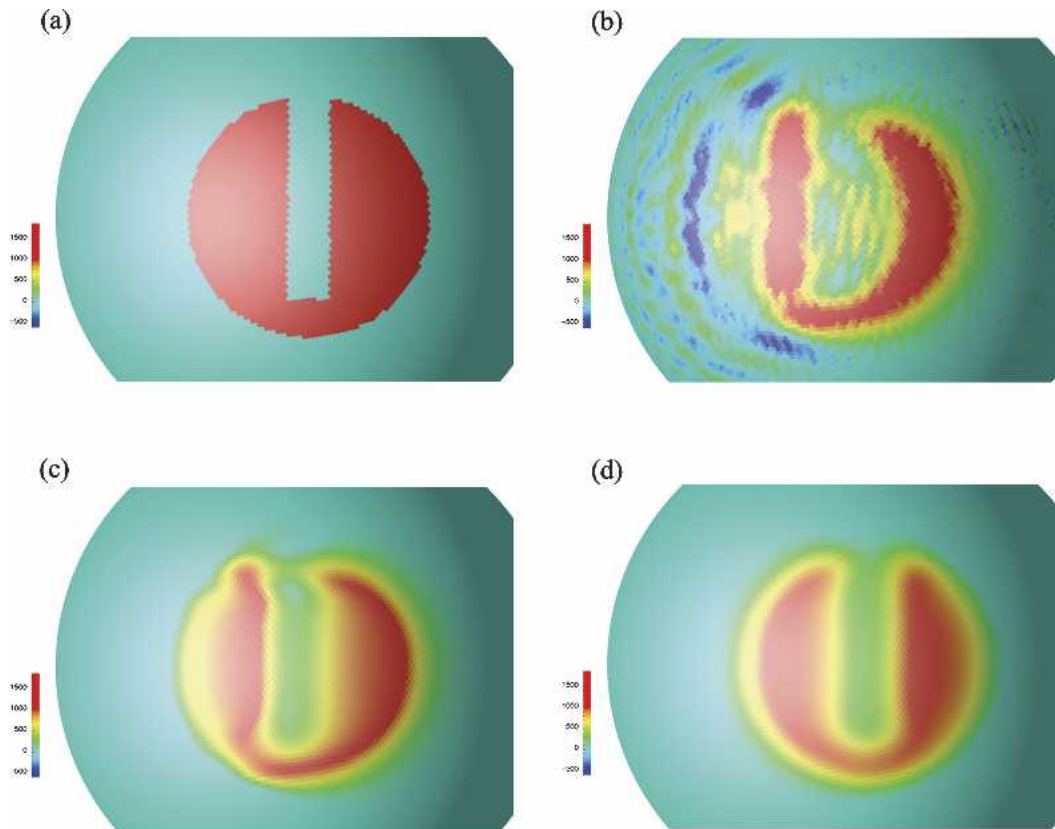


FIG. 9. Slotted cylinder thickness fields for SWTC1 with  $N = 40\,962$  after one revolution. Each plot uses the same color scale. (a) Exact solution, identical to the initial condition. (b) Centered scheme. (c) FCT. (d) Remapping.

slightly less accurate than the other two schemes at  $N = 163\,842$ .

In addition to the thickness, two passive tracers are transported:  $T_1$  and  $T_2$ . Both tracers are initially zero everywhere except within a circular region of radius  $R = \pi a/9$ , centered at  $30^\circ\text{N}$ . Since the tracers are displaced from the equator, they must pass through the midlatitude pentagons where the grid is least regular. At  $t = 0$ ,  $T_1$  in the circular region is given by

$$T_1 = T_{10}(1 - r/R), \quad (41)$$

where  $r < R$  is the distance from the center. This distribution is conical and is continuous in the tracer field, though not its first derivative. Tracer  $T_2$  is initialized with a constant value in the circular region and a discontinuity at the edge. As for SWTC1, a perfect scheme would return both tracer distributions exactly to their initial positions after 12 days. Error norms can be found using (38) and (39), replacing  $h$  with  $hT$ . Although these norms measure errors in both thickness and tracer, the tracer errors dominate. The  $L_2$  norms (not shown) for these thickness-weighted tracer fields are similar to those shown in Fig. 7. For both tracers at all

resolutions, remapping is more accurate than the centered scheme by a factor of 2. The FCT scheme is intermediate in accuracy. The convergence rates are roughly first order for  $T_1$  and slower than first order for  $T_2$ . For the  $L_\infty$  norms, no scheme is clearly best for  $T_1$ , but remapping gives the smallest errors for  $T_2$ . As in SWTC1, remapping does best at maintaining the initial shapes. The FCT solutions are somewhat ragged along the trailing edge, and the centered solutions have large oscillations.

### c. Shallow-water test case 5

SWTC5 consists of zonal flow impinging on a mountain. The mountain has the same conical shape as the  $T_1$  field defined in (41):

$$h_s = h_{s0}(1 - r/R), \quad (42)$$

where  $r < R$ , and  $h_s = 0$  elsewhere. The mountain is centered at  $30^\circ\text{N}$  with  $h_{s0} = 2000$  m and  $R = 20^\circ$ . The initial velocity, thickness, and tracer fields are the same as in SWTC2, except that  $u_0 = 20$  m s $^{-1}$ , giving a period of about 23 days for fluid parcels to circle the earth. The

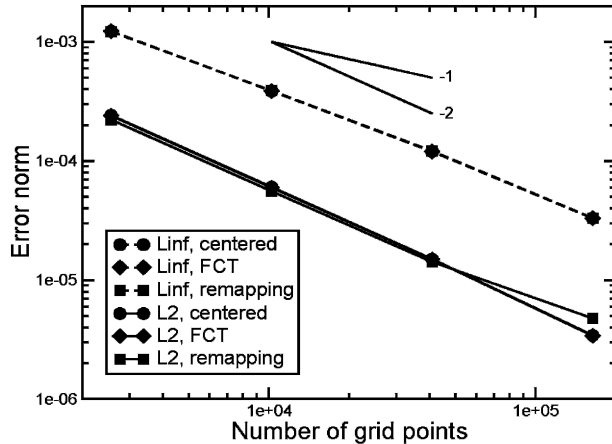


FIG. 10. SWTC2 thickness field error norms for the centered, FCT, and remapping schemes as a function of grid resolution. The  $L_2$  norm (solid lines) measures the rms global error, and the  $L_\infty$  norm (dashed lines) measures the absolute value of the largest local error. Also shown are reference lines with slopes of  $-1$  and  $-2$ , corresponding to first-order and second-order accuracy, respectively.

thickness and velocity fields change under the influence of the mountain, testing the scheme's ability to simulate geostrophic adjustment and dynamical flow. We first examine the thickness field at the end of a 15-day simulation, then discuss the conservation properties of each scheme.

The analytical solution for the thickness field is unknown but can be estimated very accurately using a high-resolution spectral model. The  $L_2$  thickness error norm is computed by comparison to the reference spectral solution and is plotted in Fig. 11 for each scheme. All three schemes have nearly the same accuracy, with a convergence rate between first order and second order. The  $L_\infty$  norm is not shown; the spectral solution does not give a valid estimate of this norm because of spectral ringing near the mountain's perimeter.

All three schemes conserve mass, mass-weighted tracer, and mass-weighted potential vorticity. The centered scheme was designed by RR to conserve three additional properties: total energy, potential enstrophy, and tracer variance. The FCT and remapping schemes do not conserve energy and potential enstrophy, and they dissipate tracer variance. Since the FCT scheme uses centered fluxes to advance the mass field, one might expect it to conserve energy and potential enstrophy as well as the centered scheme. This would be true for an FCT scheme with two time levels. The conservation of quadratic quantities is broken, however, by the modifications required to use FCT in an AB3 scheme.

Figure 12 shows how much each scheme violates con-

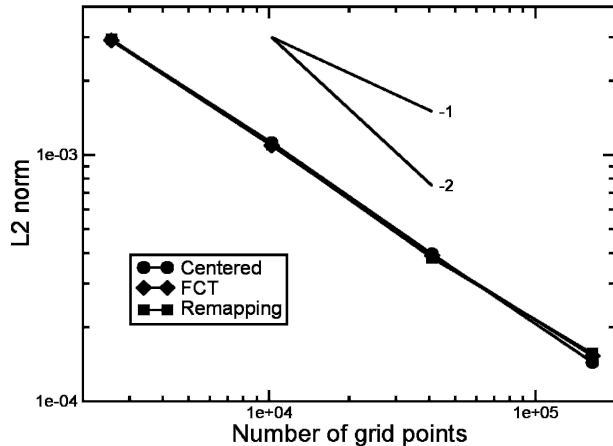


FIG. 11. SWTC5 thickness field  $L_2$  error norms for the centered, FCT, and remapping schemes as a function of grid resolution. Lines with slopes of  $-1$  and  $-2$  are shown for reference.

servation of energy and potential enstrophy in SWTC5 during the 15-day run. As expected, the centered scheme is best. At  $N = 2562$  the fractional energy conservation error with centered differencing is  $5.6 \times 10^{-7}$ , about half as large as the remapping and FCT errors. The centered scheme's energy error decreases by a factor of 2–4 with each doubling of resolution. Remapping conserves energy as well as the centered scheme for  $N = 10\,242$  but does not improve at higher resolution. The FCT energy error is nearly independent of resolution and is larger than the remapping error at the three finer resolutions. The potential enstrophy error for the centered scheme is about  $3 \times 10^{-10}$  at all resolutions, several orders of magnitude smaller than the errors given by remapping and FCT. At  $N = 2562$  the FCT enstrophy error is 15 times smaller than the remapping error. However, the remapping error is reduced by a factor of 4 with each doubling of resolution, whereas the FCT error increases slightly at finer resolution. At  $N = 163\,842$  the FCT enstrophy error is about 5 times larger than the remapping error.

Figure 13 shows how well each scheme preserves tracer variance, defined as the global sum of the area- and thickness-weighted squared tracer. The ratio of final to initial tracer variance for SWTC5 is plotted at each resolution. The centered scheme conserves variance to within roundoff error for both tracers. The percentage of tracer 1 variance preserved by remapping increases from 33% at  $N = 2562$  to 87% at  $N = 163\,842$ . For tracer 2, remapping preserves 40% of the variance at  $N = 2562$  and 84% at  $N = 163\,842$ . The FCT results are nearly identical to the remapping results, except that FCT preserves 94% of the tracer 1 variance at the finest resolution.

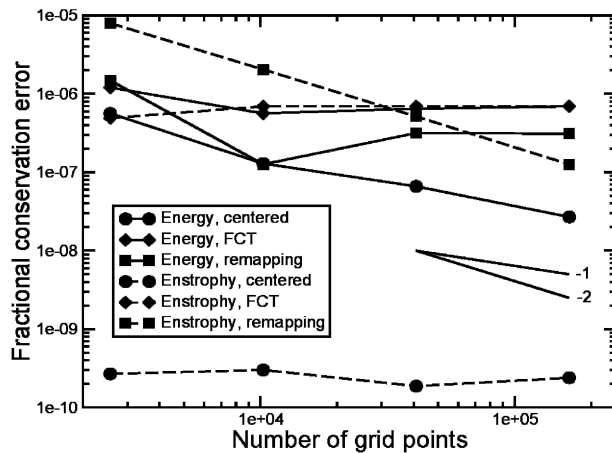


FIG. 12. Fractional conservation errors for energy (solid lines) and potential enstrophy (dashed lines) in SWTC5 for the centered, FCT, and remapping schemes, as measured by the fractional difference between the final and initial values. Lines with slopes of  $-1$  and  $-2$  are shown for reference.

#### d. Performance

The computational cost of each scheme was measured using SWTC2, as suggested by Williamson et al. (1992). Each scheme was run for 12 model hours with a time step of 50 s on a single processor of an SGI Origin 2000 computer. Figure 14 shows how the CPU time for this test case varies with the number of tracers at  $N = 2562$ . (The cost ratios are similar at higher resolutions.) With two tracers, remapping is 1.8 times as expensive as the centered scheme. The cost of the momentum solver is about the same, but the transport solver is 4.0 times as expensive for remapping. The FCT scheme with two

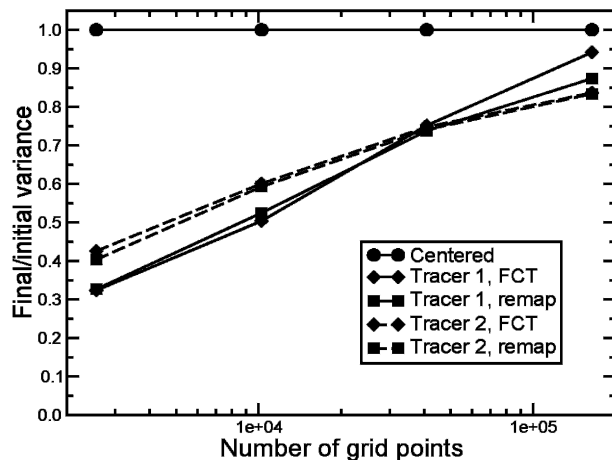


FIG. 13. Ratio of final to initial variance of tracer 1 (solid lines) and tracer 2 (dashed lines) for the centered, FCT, and remapping schemes in SWTC5. The centered scheme conserves tracer variance exactly.

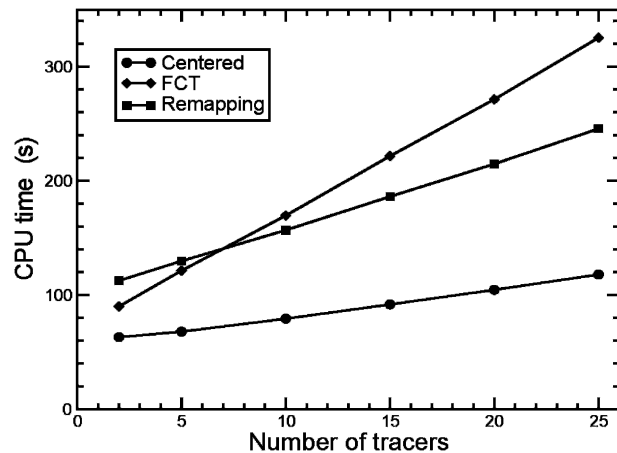


FIG. 14. Computational cost (seconds of CPU time) of the shallow-water model using the centered, FCT, and remapping schemes, as a function of the number of tracers transported. These costs are for SWTC2, run for 12 model hours on a single processor with a time step of 50 s and grid resolution  $N = 2562$ .

tracers is 1.4 times as expensive as the centered scheme for the entire model, and 2.7 times as expensive for transport alone.

The relatively expensive geometry calculations of section 3b are not repeated for each tracer. As a result, remapping scales better than FCT as tracers are added; each additional FCT tracer costs about 1.8 times as much as an additional remapped tracer. Remapping and FCT have about the same cost when seven tracers are present. With 25 tracers, remapping is 30% cheaper than FCT for transport alone and 25% cheaper for the model as a whole. The centered scheme is much cheaper than either remapping or FCT for any number of tracers. Each new tracer in the centered scheme is 2.6 times cheaper than a remapped tracer and 4.7 times cheaper than an FCT tracer.

## 6. Conclusions

Incremental remapping has been shown to be a practical scheme for solving the transport equations of the shallow-water model on a geodesic grid. To our knowledge, this is the first successful use of a DB-type remapping scheme in a fluid dynamical problem with high Reynolds number (i.e., low frictional force compared to inertial force). Previously, these schemes have been used in transport-only test problems and in sea ice models with low Reynolds number. Remapping can be adapted to a third-order Adams–Bashforth time-stepping scheme without significant violations of monotonicity, at least in the test problems studied here.

The remapping scheme was compared to the cen-

tered, second-order-accurate RR scheme and to an FCT scheme in shallow-water test cases 1, 2, and 5. For the dynamically controlled thickness fields in SWTC2 and SWTC5, all three schemes are about equally accurate, as measured by the  $L_2$  and  $L_\infty$  error norms. For passive tracers, remapping is far superior to the centered scheme, which produces large overshoots and undershoots, and is generally more accurate than FCT. Remapping preserves the shape of tracer fields better than FCT, which tends to distort solutions at the trailing edge. Remapping does not conserve total energy, potential enstrophy, or tracer variance as well as the centered scheme, which was specifically designed to conserve these properties. However, remapping conserves these properties about as well as FCT.

The main advantage of remapping compared to the RR scheme is its improved treatment of tracers. The main disadvantage is its failure to conserve higher-order quantities such as energy and potential enstrophy. However, the remapping conservation errors are relatively small: less than one part in  $10^6$  for a 15-day SWTC5 run at a resolution of  $N = 40\,962$ . If conservation of total energy and potential enstrophy were desired in addition to tracer monotonicity, one could design a hybrid scheme using centered fluxes to transport the mass field while using remapping to transport tracers. Care would have to be taken to ensure that the mass-weighted tracer fluxes were consistent with the mass fluxes. This scheme would give improved results for the shallow-water model but would be limited to flows with thick, smooth layers. For problems with thin layers and steep mass gradients, the mass would have to be limited to remain positive. In this case the centered scheme would not work, and energy and potential enstrophy would no longer be conserved.

The biggest advantage of remapping relative to FCT is its lower marginal cost per tracer. FCT is cheaper for transport of fewer than seven tracers, because of the high startup cost associated with geometric calculations in remapping. However, remapping is nearly twice as fast as FCT for each additional tracer, giving substantial savings in models that transport many tracer fields.

Remapping will next be tested in an ocean model with a quasi-Lagrangian vertical coordinate. Such a model is basically a set of stacked shallow-water models in which the layer thickness can have large horizontal gradients. Remapping will also be used for horizontal transport in a sea ice model that is being designed for a geodesic grid. Results from these experiments will be reported in future publications.

*Acknowledgments.* This work was supported by the Scientific Discovery through Advanced Computing

(SciDAC) program of the U.S. Department of Energy's Office of Science (Grant DE-FC02-10ER63163). We thank Ross Heikes for writing the FCT scheme and providing Figs. 1 and 2. We also thank Luca Bonaventura, John Dukowicz, David Randall, and two anonymous reviewers for helpful comments.

## APPENDIX

### Departure Triangles

In the following discussion, grid cells are denoted by a single letter, points by two letters, and line segments by three letters. Referring to Fig. 6, four grid cells can contribute to the departure region across each cell edge. The two grid cells bordering the edge are denoted as top ( $T$ ) and bottom ( $B$ ), and the two cells containing an endpoint of the edge are left ( $L$ ) and right ( $R$ ). The endpoints of the edge are center left (CL) and center right (CR). The four neighboring edges have additional endpoints top left (TL), top right (TR), bottom left (BL), and bottom right (BR). The departure points associated with CL and CR are DL and DR, respectively. The primary edge is CLR; the segment joining the departure points is DLR; and the four neighboring edges are TCL, TCR, BCL, and BCR. It is convenient to work in coordinate system  $X4$ , whose origin is the midpoint of CLR. The  $x$  axis points toward  $R$  along CLR; the  $y$  axis is perpendicular to CLR and points toward  $T$ .

Figure 6 shows two examples of departure regions; many other configurations are possible. In Fig. 6a, segment DLR intersects segments TCL and TCR at points IL and IR, respectively. There are four departure triangles: one in  $L$ , one in  $R$ , and two in  $T$ . In Fig. 6b, DLR intersects CLR at point IC, without entering cells  $L$  or  $R$ . There are two departure triangles: one in  $T$  and one in  $B$ . The vertices of all possible departure triangles are included in the set (CL, CR, DL, DR, IC, IL, IR).

The first step in computing the vertices of departure triangles is to locate CL, CR, TL, TR, BL, BR, DL, and DR in  $X4$  coordinates. The first six of these points can be precomputed and stored, whereas DL and DR are computed during each time step as described in section 3b. Next the slope and  $y$  intercept of DLR are computed. If DLR intersects CLR, the position of IC is found. The position of IL is determined if DL lies in cell  $L$ , and similarly for IR if DR lies in cell  $R$ . Given the locations of all potential vertices, logical tests determine the vertices of each departure triangle. The possible triangles can be divided into six types as shown in Table A1. At most four types can be present at one time. Figure 6a illustrates types 1 and 2, located in cells  $L$  and  $R$ , along with types 3a and 4a, which coexist

TABLE A1. Logical conditions and vertices for departure triangles.

Triangle type	Logical conditions	Triangle vertices
1	DLR intersects TCL or BCL	CL, DL, IL
2	DLR intersects TCR or BCR	CR, DR, IR
3a	DLR does not intersect CLR	CL, DL*, DR*
4a	DLR does not intersect CLR	CL, CR, DR*
3b	DLR intersects CLR	CL, DL*, IC
4b	DLR intersects CLR	CR, DR*, IC

when DLR does not intersect CLR. Figure 6b shows types 3b and 4b, which coexist when DLR intersects CLR. Each of the six types is associated with a distinct set of three vertices. Point DL\* refers to IL if type 1 is present; otherwise, DL\* refers to DL. Analogously, DR\* refers to either IR or DR.

## REFERENCES

- Du, Q., V. Faber, and M. Gunzburger, 1999: Centroidal Voronoi tessellations: Applications and algorithms. *SIAM Rev.*, **41**, 637–676.
- Dukowicz, J. K., and J. R. Baumgardner, 2000: Incremental remapping as a transport/advection algorithm. *J. Comput. Phys.*, **160**, 318–335.
- Durrant, D. R., 1991: The third-order Adams–Bashforth method: An attractive alternative to leapfrog time differencing. *Mon. Wea. Rev.*, **119**, 702–720.
- Giraldo, F. X., 1999: Trajectory calculations for spherical geodesic grids in Cartesian space. *Mon. Wea. Rev.*, **127**, 1651–1662.
- Heikes, R., and D. A. Randall, 1995: Numerical integration of the shallow-water equations on a twisted icosahedral grid. Part I: Basic design and results of tests. *Mon. Wea. Rev.*, **123**, 1862–1880.
- Hunke, E. C., and J. K. Dukowicz, 1997: An elastic–viscous–plastic model for sea ice dynamics. *J. Phys. Oceanogr.*, **27**, 1849–1867.
- LeVeque, R. J., 1992: *Numerical Methods for Conservation Laws*. Birkhauser Verlag, 214 pp.
- Lipscomb, W. H., and E. C. Hunke, 2004: Modeling sea ice transport using incremental remapping. *Mon. Wea. Rev.*, **132**, 1341–1354.
- Masuda, Y., and H. Ohnishi, 1986: An integration scheme of the primitive equations model with an icosahedral-hexagonal grid system and its application to the shallow water equations. *Short- and Medium-Range Numerical Weather Prediction*, T. Matsuno, Ed., Japan Meteorological Society, 317–326.
- McGregor, J. L., 1993: Economical determination of departure points for semi-Lagrangian models. *Mon. Wea. Rev.*, **121**, 221–230.
- Nair, R. D., and B. Machenhauer, 2002: The mass-conservative cell-integrated semi-Lagrangian advection scheme on the sphere. *Mon. Wea. Rev.*, **130**, 649–667.
- , J. S. Scroggs, and F. H. M. Semazzi, 2003: A forward-trajectory global semi-Lagrangian transport scheme. *J. Comput. Phys.*, **190**, 275–294.
- Randall, D. A., T. D. Ringler, R. Heikes, P. Jones, and J. Baumgardner, 2002: Climate modeling with spherical geodesic grids. *Comput. Sci. Eng.*, **4**, 32–41.
- Ringler, T. D., and D. A. Randall, 2002a: A potential enstrophy and energy conserving numerical scheme for solution of the shallow-water equations on a geodesic grid. *Mon. Wea. Rev.*, **130**, 1397–1410.
- , and —, 2002b: The ZM grid: An alternative to the Z grid. *Mon. Wea. Rev.*, **130**, 1411–1422.
- , R. P. Heikes, and D. A. Randall, 2000: Modeling the atmospheric general circulation using a spherical geodesic grid: A new class of dynamical cores. *Mon. Wea. Rev.*, **128**, 2471–2490.
- Sadourny, R., A. Arakawa, and Y. Mintz, 1968: Integration of the nondivergent barotropic vorticity equation with an icosahedral-hexagonal grid for the sphere. *Mon. Wea. Rev.*, **96**, 351–356.
- Schär, C., and P. K. Smolarkiewicz, 1996: A synchronous and iterative flux-correction formalism for coupled transport. *J. Comput. Phys.*, **128**, 101–120.
- Smith, R. D., S. Kortas, and B. Meltz, 1995: Curvilinear coordinates for global ocean models. Tech. Rep. LA-UR-95-1146, Los Alamos National Laboratory, Los Alamos, NM, 53 pp.
- Smolarkiewicz, P. K., 1991: Nonoscillatory advection schemes. *Proc. ECMWF Seminar on Numerical Methods in Atmospheric Models*, Reading, United Kingdom, European Centre for Medium-Range Weather Forecasts, 235–256.
- Stroud, A. H., 1971: *Approximate Calculation of Multiple Integrals*. Prentice-Hall, 431 pp.
- Thuburn, J., 1997: A PV-based shallow-water model on a hexagonal-icosahedral grid. *Mon. Wea. Rev.*, **125**, 2328–2347.
- van Leer, B., 1979: Towards the ultimate conservative difference scheme. V. A second-order sequel to Godunov’s method. *J. Comput. Phys.*, **32**, 101–136.
- Williamson, D. L., 1968: Integration of the barotropic vorticity equations on a spherical geodesic grid. *Tellus*, **20**, 642–653.
- , J. B. Drake, J. J. Hack, R. Jakob, and P. N. Swarztrauber, 1992: A standard test set of numerical approximations to the shallow water equations in spherical geometry. *J. Comput. Phys.*, **102**, 211–224.
- Zalesak, S. T., 1979: Fully multidimensional flux-corrected transport algorithms for fluids. *J. Comput. Phys.*, **31**, 335–362.